

1 **The Role of Gravity Waves in the Mesosphere-Lower-Thermosphere Inversion**
2 **Layers over Low-Latitude Using SABER Satellite Observations**

3 **Chalachew Lingerew^{1*}, U. Jaya Prakash Raju¹**

4 ¹Department of Physics, Washera Geospace, and Radar Science Laboratory, Bahir Dar University,
5 Bahir Dar, Ethiopia

6 *Correspondence to:* Chalachew Lingerew (chalachewlingerew@gmail.com)

7 **Abstract**

8 The Mesosphere and lower thermosphere (MLT) transitional region is a distinct and highly
9 turbulent zone of the atmosphere. A transition mesosphere region is connected with dynamic
10 processes, particularly gravity waves, as a causative of an inversion phenomenon. Understanding
11 MIL (mesosphere inversion layer) phenomena is important under the influence of atmospheric
12 waves for the understanding of middle and upper atmosphere dynamics for two primary reasons:
13 stability and energy transfer. Mesospheric inversions have been the subject of numerous
14 investigations, but their formation mechanisms are still poorly understood. In this article, an
15 attempt has been made to investigate the upper and lower inversion phenomena and their causative
16 mechanisms using long-term SABER observations in the height range of 60-100 km from 2005 to
17 2020 over a low-latitude region (3-15° N). The results indicate that the frequency of occurrence
18 rate for the upper inversion is below 40%, whereas for the lower inversion, it is below 20%,
19 indicating that the upper inversion is dominant over the lower inversion. The upper inversion exists
20 in the height range of 78-91 km with an inversion amplitude of ~20-80 k and a thickness of ~3-12
21 km, whereas the lower inversion is confined in the height range of 70-80 km with an inversion
22 amplitude of ~10-60 k and a thickness of ~4-10 km. Therein the gravity wave indicator potential
23 energy depicts high energy (below 100 J/kg) in the upper mesosphere region (85 and 90 km)
24 compared to the lower mesosphere region (70 and 75 km) with less than 50 J/kg. On account of
25 Gws, the stability criteria from Brunt-Vaisala frequency (N^2) indicate instability in the upper
26 mesosphere region with very low values relative to the lower mesosphere region. This result leads
27 us to the conclusion that a high amount of gravity wave potential energy is a consequence of the
28 high instability in the upper inversion relative to the lower inversion.

29 **Keywords.** MLT, Upper and Lower Inversions, Perturbed temperature, Causative gravity waves,
30 Potential Energy, Brunt-Vaisala frequency, Instability.

31 **Introduction**

32 The mesosphere dynamic regions act as a transition zone to the lower and upper atmospheric wave
33 processes (tidal waves, planetary waves, and gravity waves). It is a well-known fact that
34 atmospheric waves, especially gravity waves (GWs) generated from the lower atmosphere,
35 propagate into the middle and upper atmospheres, break in the mesosphere region during
36 propagation, and dissipate their energy and momentum into the background atmosphere,
37 influencing the dynamics of the mesosphere thermal structure, global atmospheric circulation,
38 variability, and even the MIL phenomenon (Lindzen, 1981; Holton, 1983). The mesospheric
39 inversion layers (MILs) are a common feature that appeared to increase the mesosphere
40 temperature variability. The MIL is a symptom (sign) of wave saturation in the mesosphere when
41 the lapse rate is less than half of the dry adiabatic lapse rate (Sica et al., 2007). Temperature
42 inversions have been omnipresent features in the mesosphere regions for decades, and they have
43 been comprehensively studied in the past by using all sorts of available techniques (e.g., lidar,
44 radar, rocket sonde, and satellite) over different geographic locations. (Sivakandan et al., 2014)
45 use the TIMED/SABER kinetic temperature data to study the occurrence of mesospheric
46 inversions and their characteristics over equatorial Indian region (0 to 10° N and 70 to 90° E) for
47 the year 2002 and 2008, which is not considering the causatives. In the present work, we
48 investigated the causatives, atmospheric waves particularly gravity waves on an inversion.

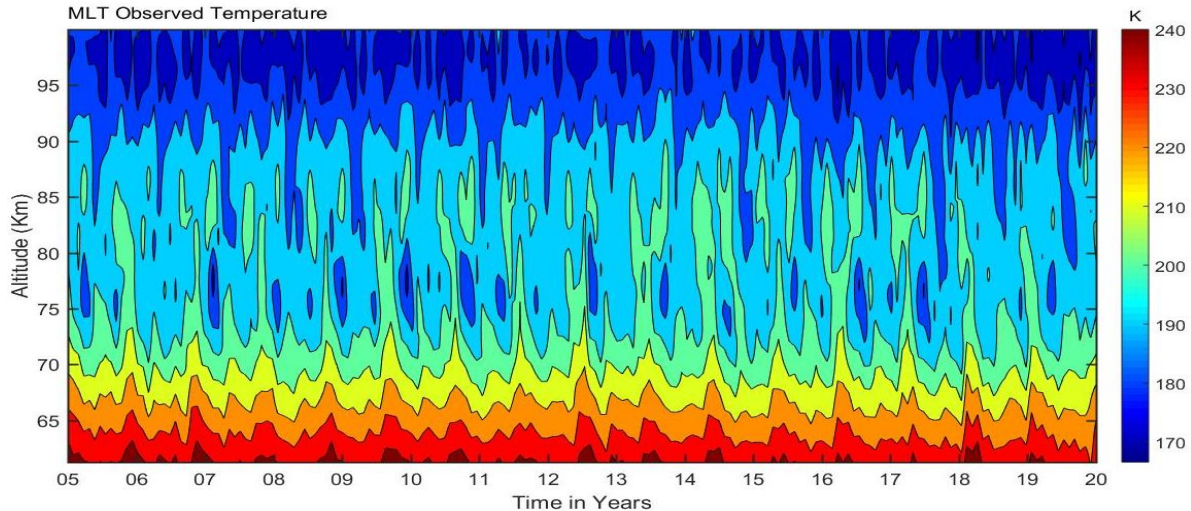
49 The gravity waves (GWs) momentum and energy deposition is thought to be the principal
50 mechanism driving large-scale circulation and coupling of distinct atmospheric layers, as well as
51 inversion phenomena (Fritts and Alexander, 2003; Lindzen, 1981; Smith, 2012). Further, the
52 gravity wave-breaking influence on mesosphere dynamics is an attempt to demonstrate their
53 impacts on the inversion phenomenon over mid and high latitudes (Gan et al., 2012; Walterscheid
54 and Hickey, 2009; Collins et al., 2011; Szewczyk et al., 2013). Observational and modeling
55 approaches have been used to investigate GWs as the causative of inversions (Fritts, 2018; Collins
56 et al., 2014; Sridharan et al., 2008; Ramesh and Sridharan, 2012; Ramesh et al., 2013, 2014, 2017).
57 The effect of gravity waves in the mesosphere inversion based on temperature variability is studied
58 particularly over the mid- and high-latitudes (Singh and Pallamraju, 2018; Fritts et al., 2018) but
59 not yet sufficiently understood. As a result, the inversion phenomenon and their causative
60 investigation is the topic of numerous studies in the mesosphere dynamics.

61 Regarding the low-latitudes, there are very less number of studies on the temporal (time) and
62 spatial (altitudinal, latitudinal, and longitudinal) variability of the mesosphere inversion
63 phenomenon associated with atmospheric waves particularly gravity wave activity. This motivates
64 us to investigate the mesosphere inversion phenomenon and its association with gravity wave
65 activity, along with stability criteria using Brunt-Vaisala frequency (N^2) over the low latitudinal
66 band (3-15⁰ N) using long-term SABER observations during 2005-2020. This is organized as
67 follows: The data and method of extracting the mesosphere inversion phenomenon are presented
68 in Section 2, and their results are described in Section 3. Finally, Section 4 presents the
69 conclusions.

70 **2. Observation and Data analysis**

71 **2.1 SABER Observation**

72 The TIMED/SABER satellite was launched on December 7, 2001, to set on an elliptical orbit at
73 an altitude of about 625 km with an inclination of 74⁰ from the equator. The SABER instrument
74 makes 15 orbits; each orbit takes 97 minutes (1.6 h) and provides about 1400 profiles per day; each
75 profile takes 58 seconds. This TIMED/SABER satellite provides temperature profiles with good
76 spatial and temporal resolution to investigate mesosphere dynamics and their atmospheric wave
77 processes. SABER temperature data has been widely used to investigate the typical thermal
78 structure and dominant dynamical processes in the mesospheric region (Garcia et al., 2008, Gan et
79 al., 2012, 2014; Bizuneh et al., 2022; Lingerew et al., 2023). For vertical temperature
80 measurement, SABER provides an accuracy of 1 to 2 K between 15 and 60 km, decreasing to 5 K
81 below 85 km, while the error increases with altitude from 6.7 K to 10 K near 100 km (Rezac et al.,
82 2015). The valuable nature of SABER observations for the study of the middle atmosphere is well
83 documented in previous research (Meriwether and Gerrard, 2004; Fechine et al., 2008; Dou et al.,
84 2009; Gan et al., 2012; France et al., 2015). In the present, we have used the latest version of
85 SABER temperature data over low-latitudes. The SABER vertical temperature profiles were taken
86 in the range of 60-100 km altitude during the period January 2005-December 2020 over (3-15⁰N)
87 latitude and (33-48⁰E) longitude regions. The monthly mean SABER temperature data of the
88 mesosphere and lower thermosphere (MLT) region is presented as shown in Figure 1. The monthly
89 mean temperature of the MLT (60-100 km) region shows a maximum temperature of 200-240 K
90 in the height range of 60-70 km, with the minimum temperature declining to around 160-180 K in
91 the height range of about 95-100 km throughout all over the period.

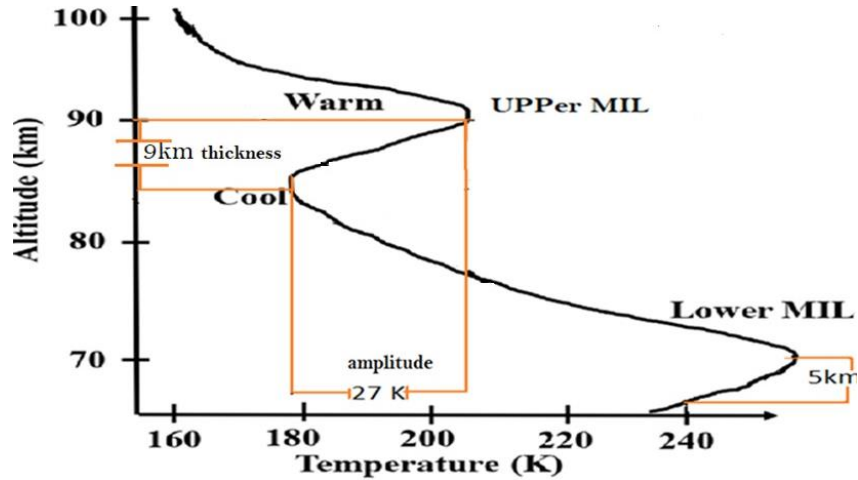


92

93 **Figure 1.** The monthly mean MLT temperature variability in the height range of 60-100 km during
 94 December 2005-January 2020 over the low-latitude.

95 **2.2 Analysis Technique**

96 The mean thermal structure of the Earth’s middle atmosphere is characterized by a negative
 97 temperature gradient. However, there are several reports showing positive temperature gradients
 98 in the mesosphere which are in contrast to the ideal situation of negative gradients (Meriwether
 99 and Gardner, 2000; Gan et al., 2012). This kind of phenomenon is known as “mesospheric
 100 inversion layer (MIL)”. MILs were identified based on following procedure outlined by
 101 Leblanc and Hauchecorne (1997) and Fechine et al. (2008) and which is briefly presented here.
 102 This procedure has been applied in many previous studies investigating the phenomenon of
 103 mesospheric inversion (Leblanc et al., 1998; Meriwether and Gardner, 2000; Duck et al., 2001;
 104 Duck and Greene, 2004; Cutler et al., 2001; Siva Kumar et al., 2001; Ratnam et al., 2003; Gan et
 105 al., 2012). Inversions of this MLT temperature are identified based on their characteristics
 106 thickness (the altitude difference between the point of warm & cool), while the temperature
 107 difference between the point of cooling and warming is termed as amplitude of the MIL
 108 (Meriwether and Gardner, 2000) as shown in figure 2, which have a positive value between the
 109 top and bottom levels.



110

111 Figure 2. Schematic of upper and lower mesospheric inversion layers shown in the temperature
 112 profile for the MLT regions (Adapted from Meriwether and Gerrard, 2004).

113 In this regard, the upper and lower mesosphere inversions were identified in the procedure of
 114 Leblanc and Hauchecorne (1997) based on the characteristics of the temperature inversions using
 115 the following criteria: (1) The bottom level of the lower and upper inversions is above 70 and 80
 116 km, and its top level of inversion is below 80 and 92 km, respectively; (2) the amplitude is
 117 considered larger than 5 K; and (3) the thickness is greater than or equal to 2 km following the
 118 procedure. Based on this sequence of temperature inversion, the diagnostic technique is applied to
 119 the SABER observed data during the period 2005-2020 over low latitudes to investigate the
 120 causative influence of atmospheric gravity waves (Gws). Inversions that satisfy the above-
 121 mentioned criteria are considered significant. As well as identifying inversions, the frequency
 122 occurrence rate (%) of mesospheric inversion layers (MILs) is derived during the period 2005–
 123 2020 in the upper and lower MLT regions. The occurrence rate of the frequency (percentage) is
 124 estimated based on dividing the monthly inversion days for each month (dates of a month) of 16-
 125 year (2005–2020) observation data.

126 The inversion of the mesosphere temperatures is related to the instabilities. Hence, we are going
 127 to derive the hourly atmospheric gravity waves via the Brunt-Vaisala frequency (N^2). Whereas
 128 another important concept to estimate the Brunt-Vaisala frequency is the potential temperature (θ),
 129 which stands for the air parcel's temperature when it is displaced adiabatically to a standard
 130 pressure level, p_0 , from the current pressure level, p , the first law of thermodynamics:

131
$$\frac{dT}{T} = \frac{R}{c_p} \frac{dp}{p} \Rightarrow \int_T^0 \frac{dT}{T} = \int_p^{p_0} \frac{R}{c_p} \frac{dp}{p} \quad (1) \text{ it yields}$$

132
$$\theta = T \left(\frac{p_0}{p} \right)^{R/c_p} \quad (2)$$

133 Therefore, the motion of the vertical atmospheric air parcel can be described by (Liu, 2011; Vadas
 134 and Fritts, 2005) as follows in equation (2.3) to calculate the Brunt-Vaisala frequency of the parcel
 135 due to the Buoyant and gravitational forces acting on the parcel:

$$136 \quad \frac{d^2s}{dt^2} = -g \frac{\rho - \rho_0}{\rho} \sin a \quad (3)$$

137 Based on the hydrostatic equation, $\rho = \rho_0$, and $p = p_0 \Rightarrow \frac{\partial p}{\partial z} = \frac{\partial p_0}{\partial z} = -g\rho_0$ (4) and the ideal gas
 138 law, $\rho = p/RT = p_0/RT$ gives the parcels motion of an equation:

$$139 \quad \frac{d^2s}{dt^2} = -\frac{g}{\rho} \left(\frac{d\rho}{dp} \frac{\partial p_0}{\partial z} - \frac{\partial \rho_0}{\partial z} \right) z \quad (5)$$

140 Following the same approach using the hydrostatic equation (4) and adiabatic equation (6)

$$141 \quad d \ln \rho = \frac{d \ln p}{\gamma}, \gamma = c_p/c_v \quad (6) \text{ yields}$$

142

$$143 \quad \frac{d^2s}{dt^2} = -\frac{g}{\rho} \left(\frac{\rho}{\gamma p_0} \frac{\partial p_0}{\partial z} - \frac{\partial \rho_0}{\partial z} \right) z = g \left(\frac{\partial \ln \rho_0}{\partial z} - \frac{1}{\gamma} \frac{\partial \ln p_0}{\partial z} \right) z \quad (7)$$

144 For the ideal gas law of $p = \rho RT$, the natural logarithm is taken for altitude, z on both sides, yielding

$$145 \quad \frac{\partial \ln \rho}{\partial z} = \frac{\partial \ln p}{\partial z} - \frac{\partial \ln T}{\partial z} \quad (8)$$

146 Then after, the potential temperature (θ) of the parcel is calculated as follows based on the equation
 147 (2):

$$148 \quad \frac{\partial \ln \theta}{\partial z} = \frac{\partial \ln T}{\partial z} - \frac{R}{c_p} \frac{\partial \ln p}{\partial z} = \frac{1}{T} \left(\frac{\partial T}{\partial z} + \frac{g}{c_p} \right) = \left(1 - \frac{R}{c_p} \right) \frac{\partial \ln p}{\partial z} - \frac{\partial \ln \rho}{\partial z} \quad (9) \text{ to derive the Parcels}$$

149 acceleration based on equations (7) to become:

$$150 \quad \frac{d^2s}{dt^2} = -g \frac{\partial \ln \theta_0}{\partial z} z \sin a = -g \frac{\partial \ln \theta_0}{\partial z} ds \cdot \sin^2 a \quad (10)$$

151 Whereas by introducing the frequency, N , with $N^2 = g \frac{\partial \ln \theta_0}{\partial z}$

152 The Brunt-Vaisala frequency, N^2 is calculated based on the following mathematical formulation
 153 used to characterize atmospheric stability.

$$154 \quad N^2(z) = \frac{g(z)}{T_0(z)} \left(\frac{\partial T_0(z)}{\partial z} + \Gamma_d \right) \quad (11)$$

155 Where g is the acceleration due to gravity, N is the Vaisala frequency, T_0 is the background
 156 temperature, estimated based on the third-order polynomial fitting, $\Gamma_d = \frac{g}{c_p}$ is the adiabatic lapse
 157 rate, and $c_p = 1004 J K^{-1} kg^{-1}$ is the specific heat capacity of the atmosphere at constant

158 pressure. When Vaisala frequency N^2 , is statically positive, the atmosphere is stable. While the
159 frequency N^2 , is negative, the atmosphere is unstable, in which the atmospheric lapse rate, $\Gamma =$
160 $-\frac{\partial T}{\partial z}$ is larger than the adiabatic lapse rate, $\frac{g}{c_p} \approx 9.5 \text{ K km}^{-1}$, the atmosphere is unstable.

161 In the meantime of estimating the Brunt-Vaisala frequency, the third-order polynomial fit of the
162 least squares has been applied to the SABER observed temperature (T) profile to estimate the
163 background temperature (T_0) following the procedure Leblanc and Hauchecorne (1997).
164 Succeeding the estimations of the perturbed temperature (T_p) from equation (2), were identified,
165 which is estimated by subtracting the background from the observed temperature data (T).

$$166 \quad T_p = T - T_0 \quad (12)$$

167 After estimating the perturbed temperature (T_p), a one-hour cut-off frequency of the low-pass band
168 filter is applied on the perturbed temperature to calculate the atmospheric gravity wave potential
169 energy (E_p) by removing the planetary and tidal wave impacts or contribution in the perturbed
170 temperature (John and Kumar, 2012).

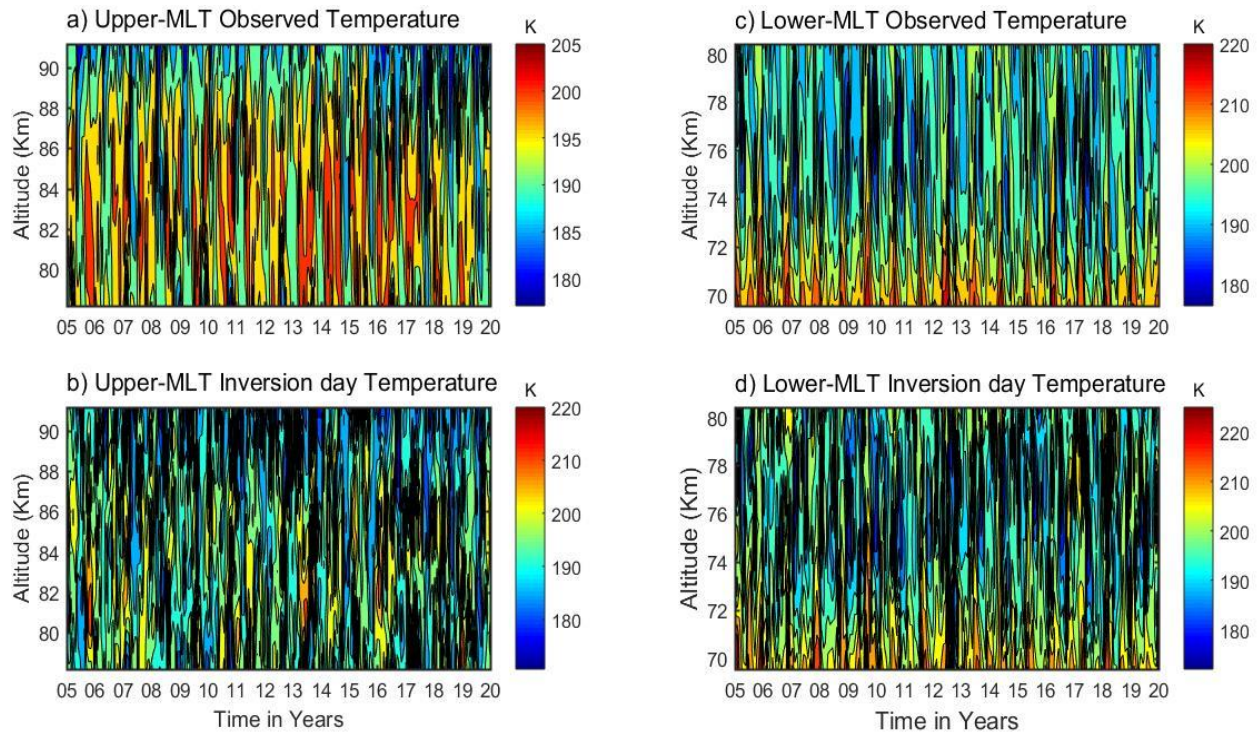
$$171 \quad E_p(z) = \frac{1}{2} \left(\frac{g(z)}{N(z)} \right)^2 \left(\frac{T_p(z)}{T_0(z)} \right)^2 \quad (13)$$

172 The potential energy of the waves is a function of altitude, z , which is utilized to determine the
173 impact of atmospheric gravity waves on atmospheric dynamics.

174 **3. Results and discussion**

175 **3.1 Identification and Characteristics of the Lower and Upper MLT Inversion**

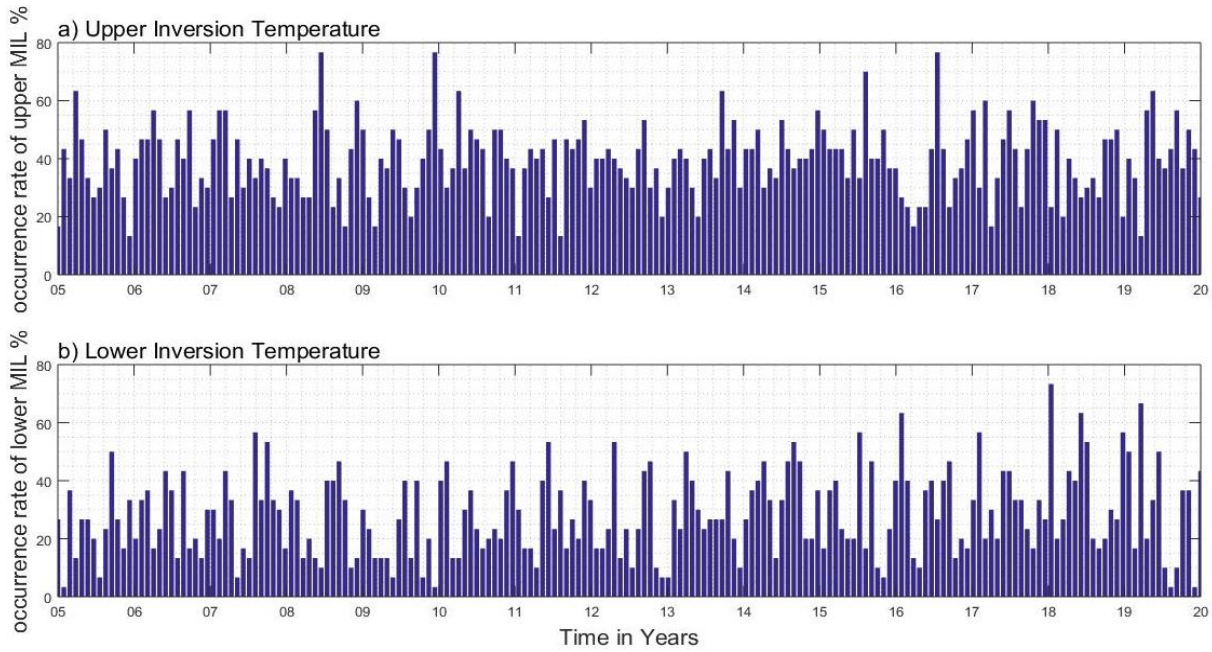
176 The daily SABER observed temperature profiles of the upper and lower mesospheres from 2005
177 to 2020 over low latitudes are depicted in the form of contours in Figure 3(a and c) in the range
178 between \sim (180-220 K). The lower panel of Figure 3(b and d) shows daily inversion temperature
179 profiles in the range of 180–225 K, indicating temperature is maximum in the inversion day
180 observed temperature at lower and upper regions when compared without considering the
181 inversion day observed temperature in Figure 3(a and c).



182
 183 **Figure 3.** The upper and lower mesosphere observed temperatures in the first horizontal panel at
 184 (a and c) with their inversions in the second horizontal panel at (b and d).

185 The upper panel on the left side of Figure 3(a) represents the upper mesosphere observed
 186 temperature, which is depicted in the range $\sim(180-205\text{ K})$ at the height around $\sim 80-90\text{ Km}$, and
 187 the right upper panel of Figure 3(c) represents the lower mesosphere observed temperature in the
 188 range around $\sim(180-220\text{ K})$ at the height around $\sim 70-80\text{ Km}$. Whereas, Figure 3(b) depicts an
 189 upper-temperature inversion about $\sim(180-220\text{ K})$ at an altitude of $\sim(80-90\text{ Km})$, while Figure 3(d)
 190 shows a lower-temperature inversion about $\sim(180-225\text{ K})$ at a height of $\sim(70-80\text{ Km})$, indicating
 191 a temperature gradient is occurred from negative to positive due to external or internal drivers,
 192 which might be atmospheric gravity waves, chemical reactions or solar radiations. The first
 193 observation of MIL was carried out by a rocket-falling experiment, which shows temperature
 194 inversion layers have been normally detected with maximum values in the mesosphere and lower
 195 thermosphere (Schmidlin, 1976). Our findings of the lower inversions in the range of (70-80 km)
 196 tend to approach the reports by Sivakumar et al. (2001), which show that the base of the lower
 197 mesospheric inversion layer (MILs) lies in the range of (73-79 km), as well as the Gan et al. (2012)
 198 seasonal variations of MIL in the planetary waves as a caustic over low-latitudes using the
 199 SABER observations. Whereas Sivakandan et al., (2014) also investigated the lower and upper

200 mesospheric inversions in the altitudinal ranges from 60-105 km over low latitudinal regions,
 201 which nearly coincides with our work results.

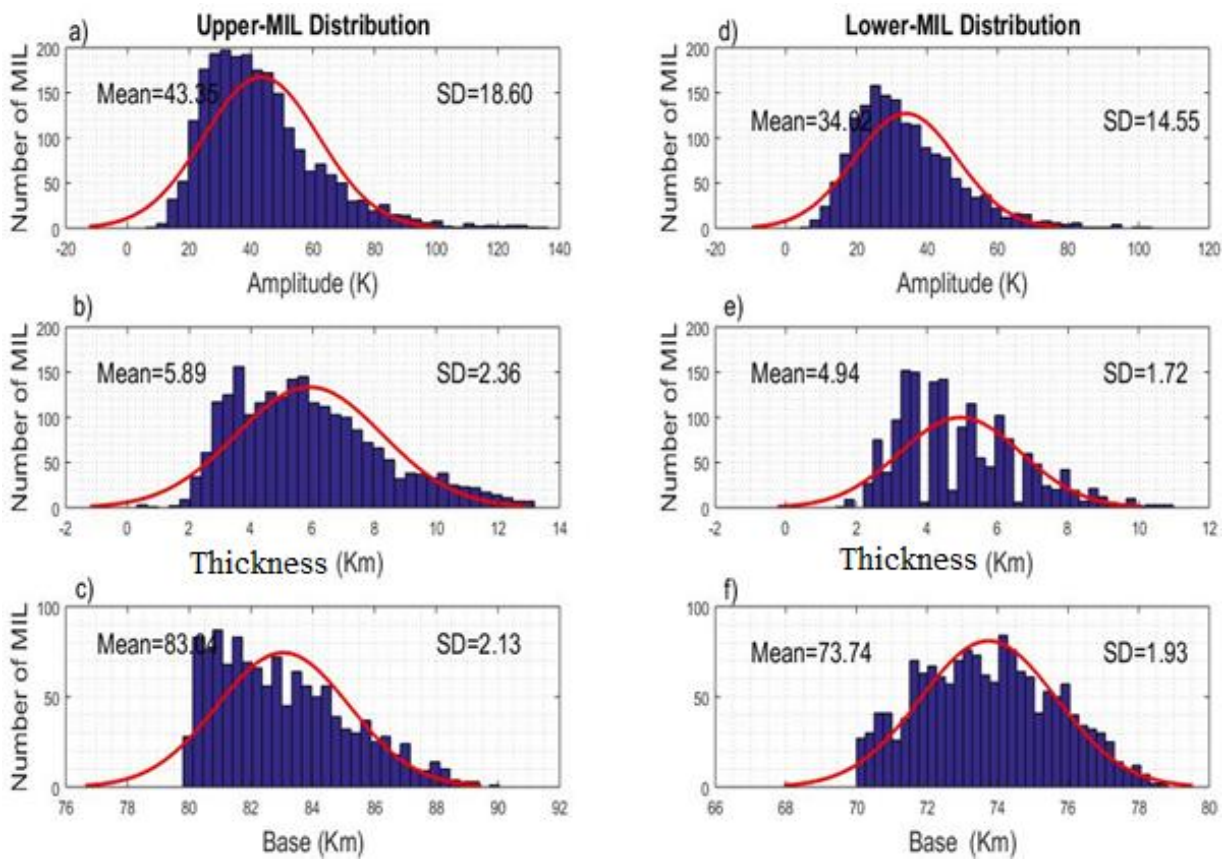


202
 203 **Figure 4.** The frequency occurrence rate (percentage) of the (a) upper and (b) lower inversion
 204 temperatures during 2005-2020 over low latitudes.

205 The frequency occurrence rate (%) of mesospheric inversion layers (MILs) were investigated as
 206 displayed in the form of a histogram in Figure 4(a) for the upper MIL and in Figure 4(b) for the
 207 lower MIL. The mean frequency occurrence rate of the upper inversion is approximately below
 208 40%, whereas their maximum occurrence rate of inversion lies between 60% and 78%, particularly
 209 in the years 2008, 2010, and mid-2016. While the mean frequency occurrence rate of the lower
 210 inversion is below 20%. As a whole, the occurrence rate of the upper inversion is relatively high
 211 compared with the lower inversion, which could be related to atmospheric wave activities,
 212 particularly gravity wave activity. In this regard, Hauchecorne et al. (1987) and France et al. (2015)
 213 show the impacts of Gws on the upper and lower mesosphere inversion variability. Not only this,
 214 Gan et al. (2012) also found the seasonal variation of MILs over the low latitudes under the
 215 causative planetary waves. As those previous scientific results of the occurrence rate the inversions
 216 of the lower and upper MLT regions were investigated based on their characteristics amplitude
 217 and thickness in Figure 5.

218 Before examining the effects of Gws on the MLT regions of an inversion, Figure 5 depicts the
 219 inversions of mesosphere temperature variability in terms of base height, amplitude, and thickness.

220 The frequency occurrence of amplitude, thickness, and base height of inversion variability in the
 221 form of the histogram along with the best-fit red lines of the Gaussian distribution are presented
 222 in Figure 5. The observed distributions coincide with Gaussian curves (best fits), indicating that
 223 the number of MILs is distributed over their attributes according to normal laws, implying that the
 224 representations are real-valued random variables. Figure 5 of the left vertical column, three rows
 225 represent a histogram of (a) amplitude, (b) thickness, and (c) the base of the upper MIL
 226 phenomenon, along with their statistical metrics mean and standard deviations (SD). Whereas the
 227 corresponding three rows of the right vertical column represent (d) amplitude, (e) thickness, and
 228 (f) the base of the lower MIL phenomenon.



229
 230 **Figure 5.** Histogram occurrence of mesosphere inversions. The first vertical panel represents the
 231 upper inversion distribution of (a) amplitude, (b) thickness, and (c) base, and the corresponding
 232 distribution in the second vertical panel is the lower inversion of (d) amplitude, (e) thickness, and
 233 (f) base over the low latitude during the period 2005–2020.

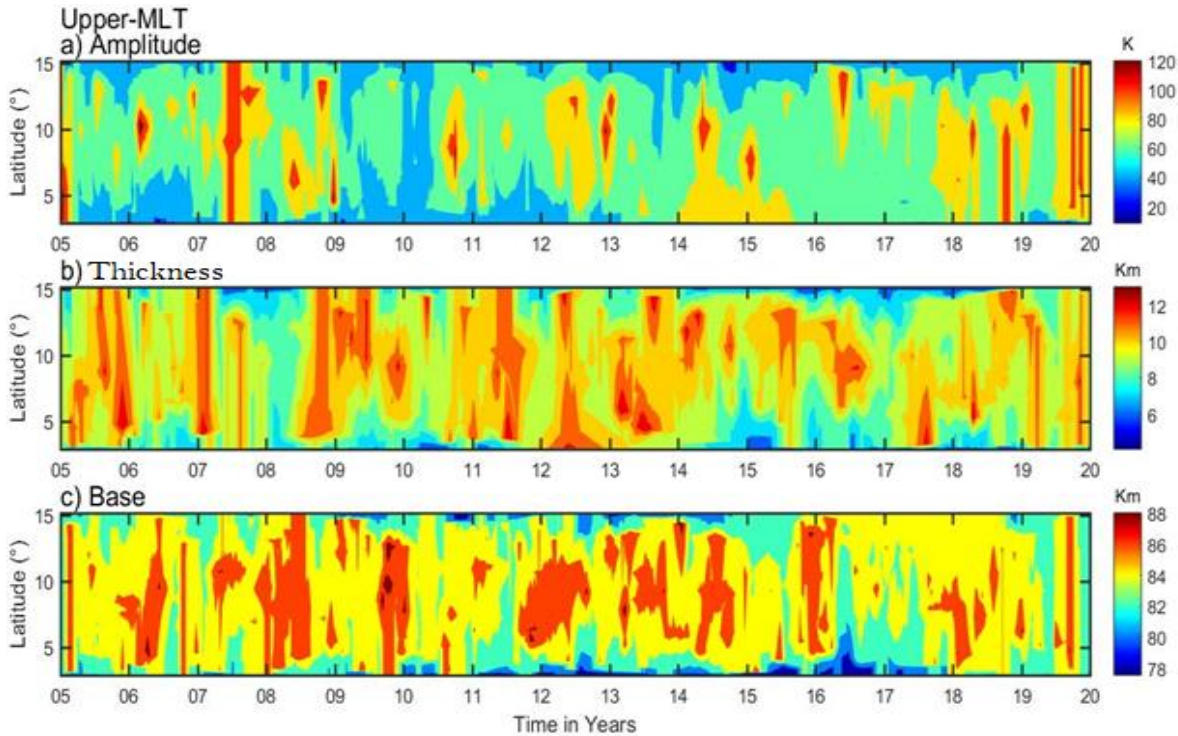
234 The amplitude of upper inversion variability in the left vertical panel in Figure 5(a) exists in the
 235 range between 20 and 80 K, with a peak value of 38 K following a Gaussian distribution with large

236 standard deviations (SD), 18.6. The thickness of the inversion layer for upper MILs has existed in
237 the range of 3-9 K, with the most probable value of 5.5 K and a low standard deviation 2.3 of
238 (Figure 5(b)). The base height of the upper MIL in Figure 5(c) ranges from ~80 to 90 km, with a
239 peak value of a large number of upper mesospheric inversions occurring at a base height of around
240 83 km in a lower standard deviation (SD) 2.13. The number of upper inversions all over the period
241 2005–2020 at a height of 82 km is the highest relative to the rest in the range between 80 and 90
242 km. Such maximum mean to fit of Gaussian distribution may be the reason for the gravity wave
243 breaking is that it dissipates energy as a causative factor for an inversion, while the wave generated
244 from the lower to the upper atmospheric region as well as the impacts of the solar flux generated
245 from the upper solar system. Whereas, the lower inversion amplitude is depicted in the range
246 between 10 and 60 K with a peak of 25 K and standard deviations (SD) 14.5 of in Figure 5(b) in
247 the right vertical panel. The thickness of an inversion has appeared in the range of 3-8 Km, with
248 the most probable value of 3.8 Km and a low standard deviation (SD) 1.72 of (Figure 5(d)). The
249 base height of the lower inversion of Figure 5(f) is in the range of 70 and 80 km, with a peak value
250 of around 74 km, showing a lower standard deviation (SD) of 1.93. In the earlier investigation,
251 from the Indian sector, Sivakandan et al. (2014) reported amplitudes in the range (14–39 K) during
252 2002 and (15–42 K) in 2008, whereas their thickness was in the range of (2.7–7.5) during 2002
253 and (2.8–7.3) in 2008 to characterize the mesospheric inversion variability under the influence of
254 solar flux, which agrees well with the present investigation. This comparison reveals that there is
255 no significant variation in characterizing the mesosphere inversion based on amplitude and
256 thickness over the low-latitude region in the altitude range of 60 to 90 km.

257 **3.2 Latitudinal Variations of Mesospheric Inversion Layers (MILs)**

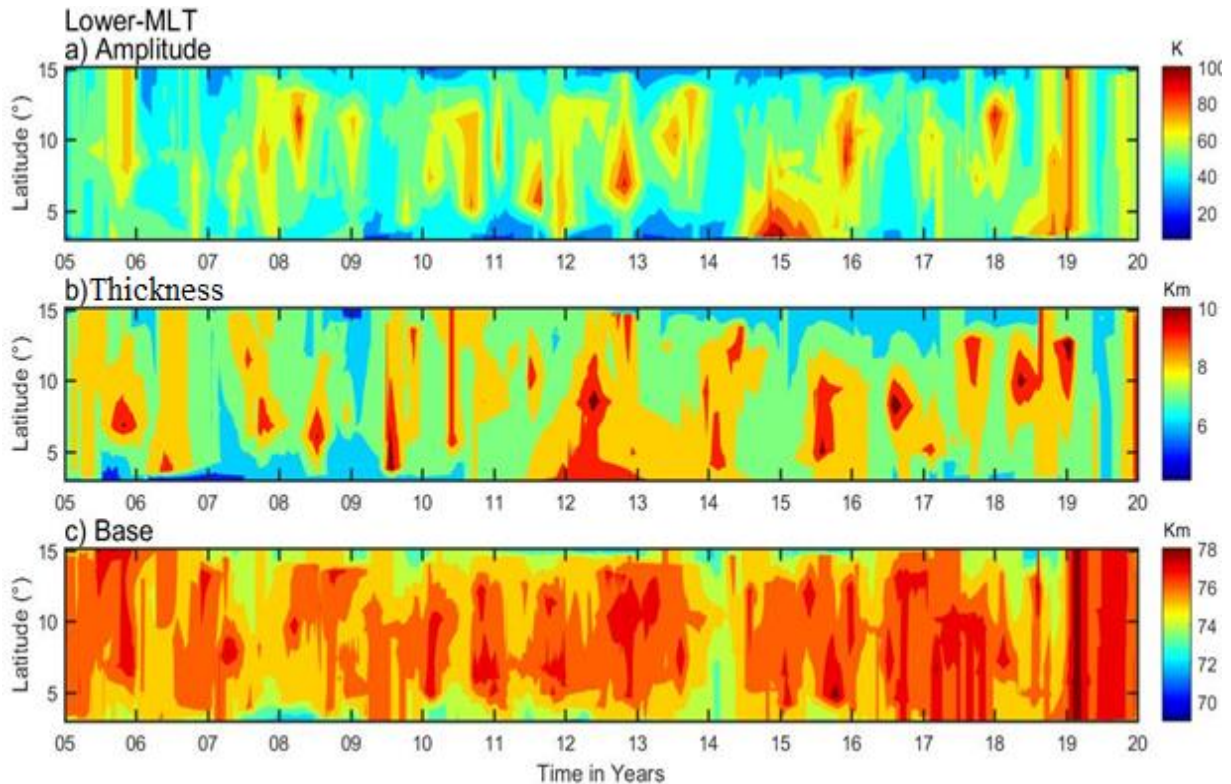
258 In this section, the spatiotemporal (latitudinal-time) variability of the upper and lower mesosphere
259 inversion phenomena is characterized in the contour plots of time vs. latitude in Figures (6 and 7)
260 respectively, based on amplitude, thickness, and base height over the low-latitude band (3-15⁰)
261 during 2005–2020. The Upper MILs phenomenon is observed around 80–90 km, with the
262 maximum amplitude in the range of 90–120 K over the latitude bands (5-12⁰N) during 2005, 2007,
263 mid-2011, 2013, 2015, 2016, mid-2019, and 2020 (Figure 6(a)). The inversion thickness depicted
264 in the second horizontal panel, as shown in Figure 6(b), is displayed with a maximum range of
265 ~(8–12 Km) over the entire latitudinal region (3-15⁰N). Figure 6(c) displays the relative maximum

266 inversion base height around $\sim(84-88 \text{ Km})$ in the latitudinal range between 4 and 14^0 N during
 267 2006, 2008, 2010, 2012, 2016, and 2018.



268 **Figure 6.** The daily upper inversions ($\sim 80-90 \text{ km}$) of (a) amplitude, (b) thickness, and (c) base
 269 height during 2005-2020 over latitudinal variation.
 270

271 Similarly, the latitudinal variations of the lower inversion (MILs) phenomenon based on their
 272 characteristics amplitude, thicknesses, and base height are depicted in the form of contour plots of
 273 time vs latitude in Figure 7(a, b, and c), respectively, over an altitudinal range around $\sim(70-80 \text{ km})$.
 274 The lower inversion amplitude is depicted in the range of $\sim 30-60 \text{ k}$ over all latitudinal bands except
 275 the maximum range of $\sim(80-100 \text{ k})$ during 2013, 2015, 2016, and 2019 in different latitudinal
 276 regions enclosed in the range between 5 and 14^0 N . Figure 7(b) displays the inversion thickness of
 277 5-7 km over the entire latitude band, except for the maximum thickness of 8-10 km. The inversion
 278 of base height (76-80) is depicted in Figure 7(c) over all latitudes and periods except 2008, 2014,
 279 and mid-year 2018 with maximum base height. Figures 6 and 7, clearly show that the high
 280 amplitude and thickness of the upper inversion in comparison with the lower inversion indicate a
 281 highly dynamic phenomenon over the upper mesosphere region.



282 **Figure 7.** Same as Figure 5, but for the lower mesosphere inversions (~70- 80 km).
 283

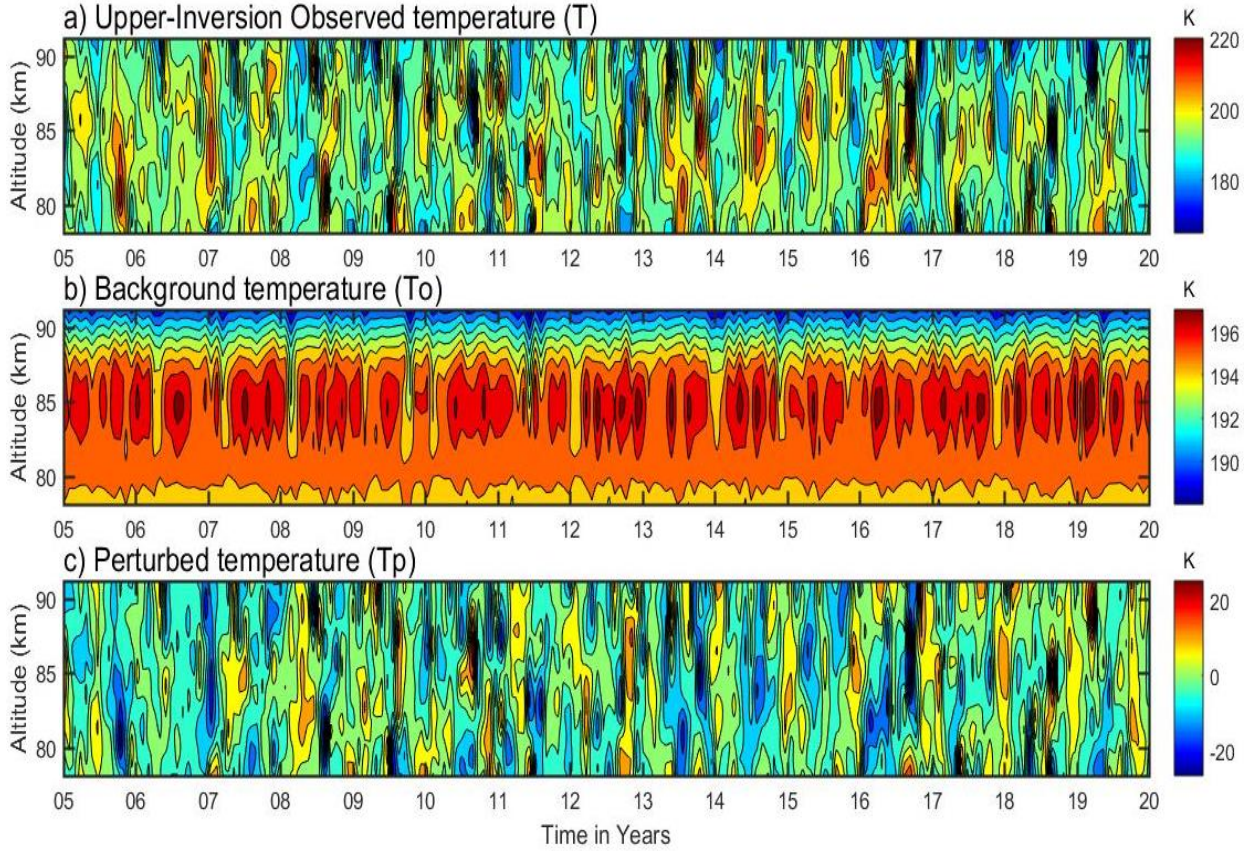
284 From Figures 6 and 7, it is observed that the upper inversion amplitude and thicknesses show high
 285 values in comparison with the lower inversion, indicating a highly dynamic phenomenon over the
 286 upper mesosphere region. Satellite measurements have a significant contribution to the
 287 information on latitudinal variations in MILs. The global climatology of MILs observed by
 288 TIMED/SABER shows that MILs also occur at low latitudes (Gan et al., 2012).

289 **3.3 Separations of the Perturbed Temperature in the Mesosphere Region**

290 The perturbed temperature profiles (T_p) in the upper and lower mesosphere inversions during the
 291 period of 2005-2020 can further be used to calculate their factors' potential energy of gravity waves
 292 and the Brunt-Vaisala frequencies (N^2). The procedure for calculating perturbation temperature
 293 (T_p) is mentioned in the methodology part.

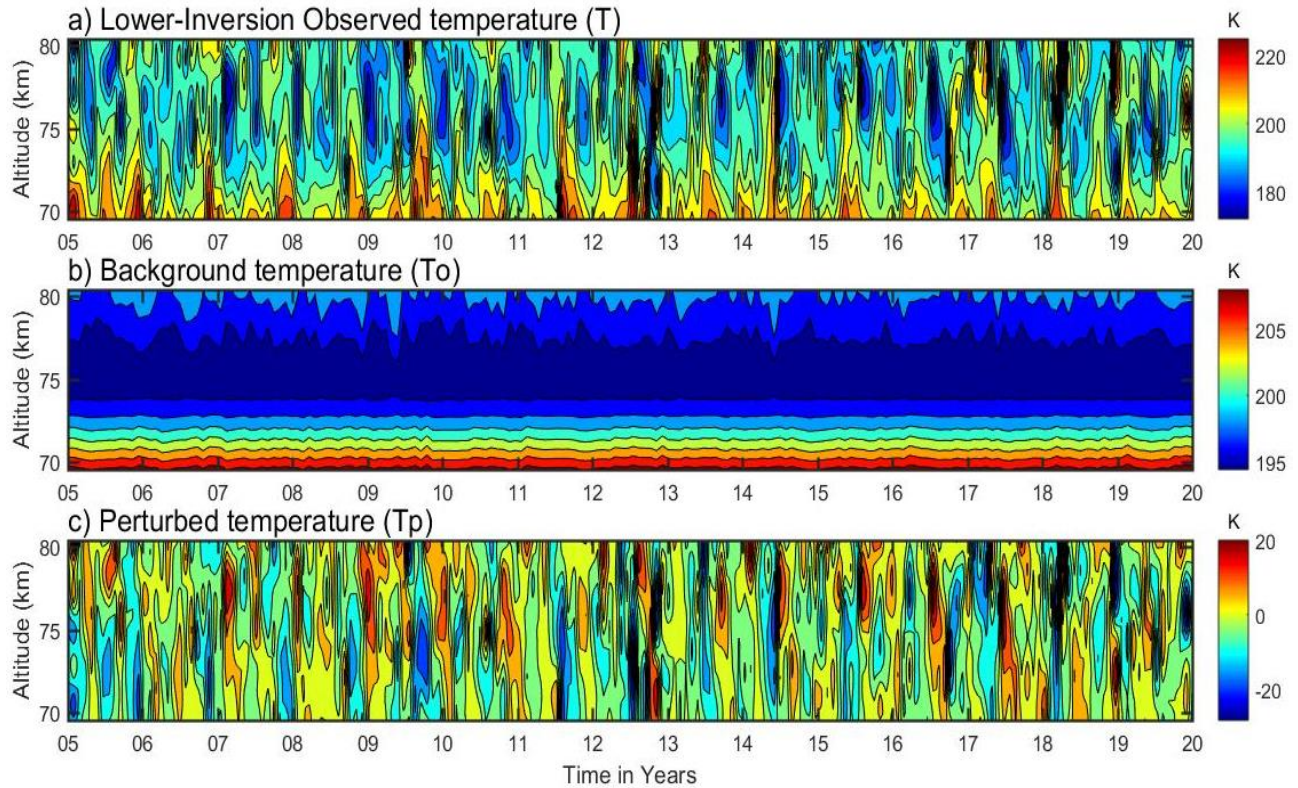
294 First, the upper-temperature inversion profiles are identified in the MLT region during the entire
 295 observational period of 2005-2020, as displayed in the contour plot of Figure 8(a). It is noted that
 296 the observed temperature is in the range of ~170-220 K with less detectable variability. Based on
 297 this inversion temperature profile, the background temperature (T_0) is calculated by applying a 3rd-
 298 order polynomial fit as shown in the corresponding contour plot of Figure 8(b). This background

299 temperature displays identifiable periodic variability in the range of ~195-197 K around ~82-87
 300 km. While the perturbed temperature profiles (T_p) are based on the difference between the
 301 observed inversion temperature (T) and the corresponding background temperature profiles (T_o),
 302 they display in the range of -25 to +25 K, as shown in Figure 8(c).



303 **Figure 8.** The upper mesosphere temperatures in the vertical panel are: (a) inversion day observed
 304 temperature; (b) background temperature; and (c) perturbed temperature in the upper mesosphere
 305 region.
 306

307 A similar procedure has been applied to calculate the perturbed temperature (T_p) as well as the
 308 observed and background temperature from 2005 to 2020 in the lower mesosphere region, and
 309 their corresponding contours are displayed in Figure 9(a-c). The observed temperature of lower
 310 inversion in Figure 9(a) depicted a range of ~170-220 K and the background temperature of lower
 311 inversion in the range of ~ 195-210 K with their maximum values of ~200-210 K over the height
 312 of ~70-72 Km as shown in Figure 9(b). Whereas the perturbed temperature in Figure 9(c) is
 313 presented in the range between -25 and 20 K. It is noted that the upper mesosphere perturbed
 314 temperature is at its maximum compared to the lower mesosphere region, which may be due to a
 315 high dynamic phenomenon.

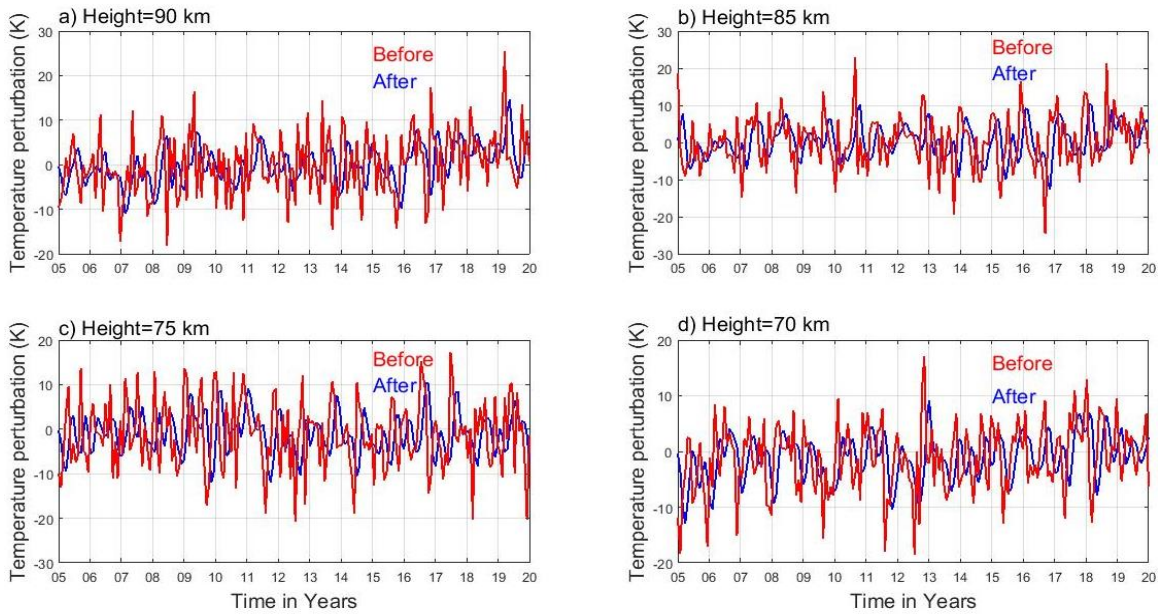


316
317 **Figure 9.** Same as Figure 7, but for the lower mesosphere atmospheric region.

318 **3.4 Effects of Gravity Waves on Mesosphere Inversions and Associated Instability**

319 Atmospheric waves (gravity waves, planetary waves, and tidal waves) exist in different layers of
 320 the atmosphere and are generated by different mechanisms. Gravity waves are of local or regional
 321 dimensions, whereas the other two waves are of global extent. This dynamical gravity wave
 322 motion is a restoring force of gravity acting downward and buoyancy acting upward on vertically
 323 displaced air parcels from the troposphere/stratosphere through the upper thermosphere. These
 324 propagated gravity waves can be distributed from their source regions across the atmosphere and
 325 become saturated at the critical upper atmospheric level, particularly over the low latitudes.
 326 Thereby, the vertically propagated waves were breaking and dissipating to transfer their energy
 327 and momentum into the atmospheric background field, thus considerably affecting the structure
 328 and variability of the atmosphere, as shown in Figure 11, as well as the results of (Holton et al.,
 329 2003; Holton and Hakim, 2013) waves potential energy affecting the atmospheric temperature
 330 inversions. The gravity wave propagation at the saturation stage is broken in the upper region to
 331 dissipate their energy, which impacts the normal mesospheric temperature by increasing its
 332 temperature with elevation, known as an inversion. This is the reason the gravity wave potential
 333 energy is connected with an inversion.

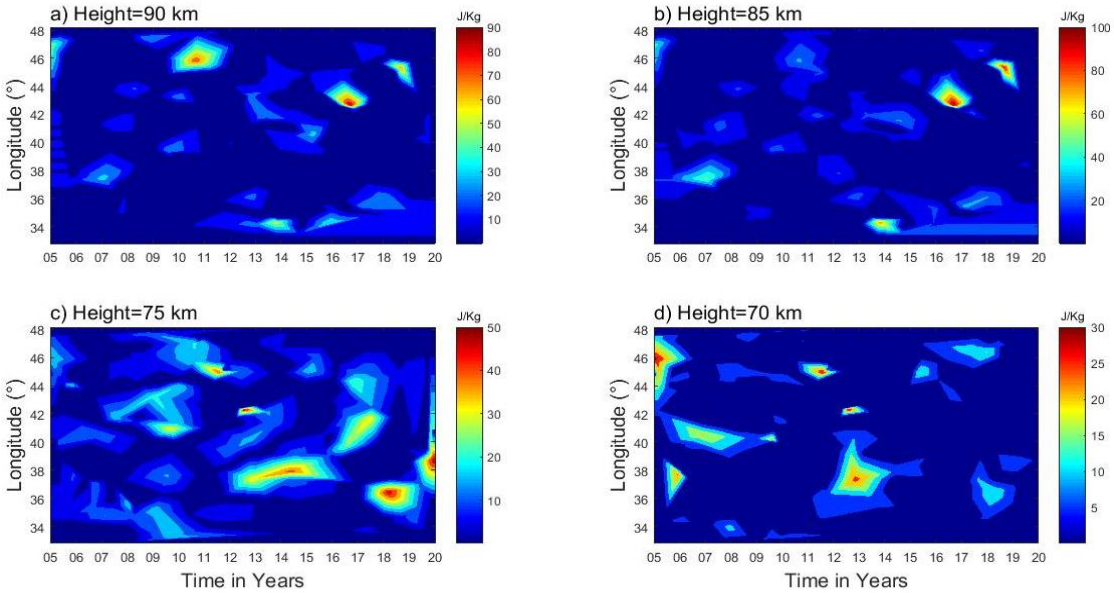
334 In this section, an attempt has been made to investigate the longitudinal variability of gravity
 335 waves' contribution to the mesospheric inversions (MILs) phenomenon by calculating potential
 336 energy and their instability based on Brunt-Vaisala frequency (N^2) using perturbed temperatures.
 337 Before deriving the waves' potential energy from the perturbed temperature (T_p), a one-hour
 338 interval cut-off-frequency of low-pass band filter is applied on a perturbed temperature (T_p) during
 339 the period 2005-2020 at selected heights of 90, 85, 75, and 70 km, as depicted in Figure 10 (a, b,
 340 c, and d). The reason behind using the low-pass band filter is to eliminate/remove the unwanted
 341 influence of long-period oscillations on an inversion such as tidal or planetary waves from the
 342 gravity wave (Gw). The effects of the low-pass band filter are visible in Figure 10(a and b) for the
 343 upper mesosphere region at 90 and 85 km and in Figure 10(c and d) for the lower mesosphere
 344 region at 75 and 70 km. The amplitude of the perturbed temperature is reduced to the range around
 345 $\sim(-10$ to 10 K), and the data is smoothed by eliminating higher frequencies.



346
 347 **Figure 10.** Perturbed temperature profiles before (red color) and after (blue color) applying the
 348 low-pass band filter for the upper (85 and 90 km) and lower (70 and 75 km) regions.

349 By using the time series of filtered perturbed temperature data at selected heights of 90, 85, 75,
 350 and 70 km, the potential energy (E_p) is constructed based on the formula mentioned in the
 351 methodology section, since the gravity wave activity is projected by the potential energy
 352 calculation as described from numerous authors (Tsuda et al., 2000; Wang and Geller, 2003; Liu
 353 et al., 2014; Thurairajah et al., 2014). The spatiotemporal variability of gravity wave potential

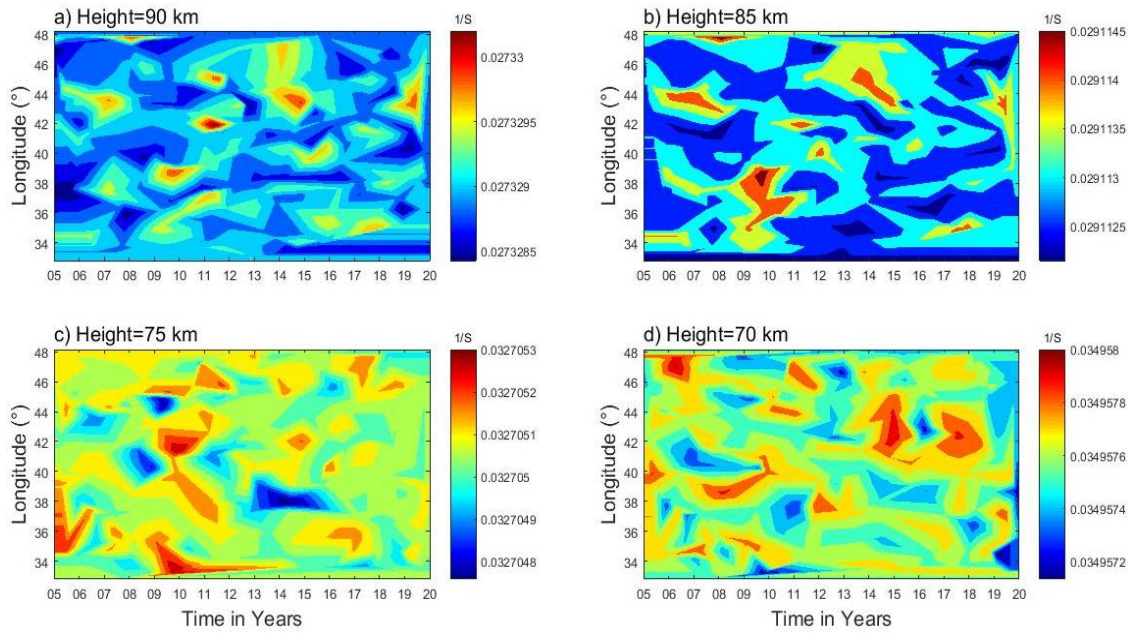
354 energy is shown in Figure 11(a and b) for the upper mesosphere region at (90 and 85 km) and
 355 Figure 11(c and d) for the lower mesosphere region at (75 and 70 km).



356
 357 **Figure 11.** Gravity wave potential energy for the upper (85 and 90 km) and lower (70 and 75
 358 km) mesosphere regions.

359 In this investigation, the maximum gravity wave potential energies were observed in the range of
 360 around $\sim 70\text{--}90$ J/kg over the longitudinal regions of $45\text{--}47^\circ\text{E}$, 43°E , and 44°E during 2011, 2017,
 361 and 2019 (Figure 11(a)) for upper mesosphere inversions at 90 km, whereas the potential energy
 362 of gravity waves around $\sim 10\text{--}60$ J/kg is presented all over the longitudinal region from $33\text{--}48^\circ$
 363 E. While the maximum potential energy $\sim (70\text{--}100$ J/kg) is observed as shown in Figure 11(b) over
 364 the longitudinal (340 , 440 , and 460) regions during 2014, 2016, and 2018 at 85 km. The minimum
 365 potential energy of gravity wave between 20 and 70 J/kg appears over the longitude ($33\text{--}48$)
 366 regions. However, Figures 11 (c and d) show the lower MLT regions of gravity wave potential
 367 energy at 75 and 70 km, respectively. At a height of 75 km allocated in Figure 11(c) is a relative
 368 maximum potential energy appeared in the range of 40-50 J/kg over the longitudinal (46° , 42° , 40° ,
 369 37° , 36° , and 38°) region during 2011, 2012, 2017, 2013–2015, 2018, and 2020. Similarly, Figure
 370 11(d) depicts the gravity wave potential energy in the range of 2–30 J/kg for the lower MLT region
 371 at 70 km over the longitudinal region ($33\text{--}48^\circ$). Out of which, the maximum potential energy of
 372 25-30 J/kg is found in a certain longitude region over a while. Many of possible mechanisms have
 373 been suggested for the cause of lower inversions; nonlinear interactions between GWs and tides
 374 (Liu and Hagan, 1998), and chemical heating (Meriwether and Mlynchzak, 1995) including GW

375 breaking (Hauchecorne et al., 1987). The role of gravity wave propagation and dissipation has
 376 been accepted as the dominant wave forcing in the MLT region (Lindzen, 1981; Holton, 1983),
 377 which affects the middle and upper atmospheric inversion. It is also understood that tides,
 378 planetary waves, and chemical processes are affects the middle atmospheric variability as well as
 379 gravity waves (Sivakandan et al., 2014). However, gravity waves are multi-scale in nature; small-
 380 scale waves may contribute predominantly to instability, and turbulence in the MLT dynamic
 381 region (Liu and Meriwether, 2004; Szewczyk et al., 2013).
 382 Hence, investigating MIL phenomena is important for the understanding of MLT atmosphere
 383 dynamics for two primary reasons: stability and energy transfer. As a result, an attempt has been
 384 made to examine the contributions of gravity waves to the MLT region's instability (MIL
 385 phenomenon) based on the Brunt-Vaisala frequency. The spatiotemporal variability of Vaisala
 386 frequency is displayed in the contour Figure 12(a and b) for the upper mesosphere region (90 and
 387 85 km) and Figure 12(c and d) for the lower mesosphere region (75 and 70 km). Based on the
 388 Brunt-Vaisala frequency, N₂, the upper MLT region is unstable (~0.027) at 90 km and (~0.029) at
 389 85 km maximum relative to the lower inversion instability at 75 km (~0.033) and 70 km (~0.035).
 390 Hauchecorne et al., (1987) described a model in which a succession of breaking GWs would
 391 generate the MIL through the gradual accumulation of heat as a cause of instability.



392
 393 Figure 12. Brunt-Vaisala frequency (N²) profiles for the upper (85 and 90 km) and lower (70 and
 394 75 km) mesosphere regions.

395 **4. Summary**

396 In this article, 16 years of SABER mesosphere temperature profiles are utilized to investigate the
397 MIL phenomenon and its causative mechanism through gravity wave potential energy (P_E) and
398 instability criteria of Brunt-Vaisala frequency (N^2) over low latitude bands. The observational
399 conclusions from this chapter are drawn as follows:

- 400 ✓ The occurrence rate of the upper mesosphere inversion frequency is maximum relative to the
401 mean occurrence rate of the lower mesosphere inversions.
- 402 ✓ Based on the analysis of frequency of occurrence on mesospheric inversion layer (MIL)
403 characteristic features, it is revealed that the most probable value for upper inversion amplitude
404 is 38 k, inversion layer thickness is 5.5 km, and the base height is 78 km. Whereas the lower
405 inversion amplitude is 25 K, the inversion layer thickness is 3.8 km, and a base height of 73
406 km.
- 407 ✓ The gravity wave indicator potential energy depicts high energy at the upper mesosphere
408 region compared to the lower mesosphere region.
- 409 ✓ The result concludes that the observation of high potential energy in the upper mesosphere
410 region is due to the deposition of high energy and momentum at the background temperature
411 by gravity wave breaking, which could influence the dynamics of the inversion phenomenon
- 412 ✓ The stability criteria at the mesosphere region are indicated by Brunt-Vaisala frequency (N^2),
413 which shows low values at the upper mesosphere region relative to the lower mesosphere
414 region, leading to the conclusion that the high potential energy at the upper mesosphere region
415 is due to the instability over that region, which gives rise to large inversion phenomena.
- 416 ✓ In general, we concluded that the processes in the atmosphere vary from region to region. As
417 a result, the atmospheric state varies significantly with altitude as well as from place to place
418 and time to time.

419 ***Data availability.*** The SABER data are freely available via the link at [http://saber.gats-inc.com/](http://saber.gats-inc.com/index.php)
420 [index.php](http://saber.gats-inc.com/index.php).

421 ***Author contribution.*** Chalachew Lingerew: data curation, investigation, software, visualization,
422 writing the original draft, and writing review. U. Jaya Prakash Raju; supervision, and editing.

423 **Competing interest.** The authors declare that they have no conflict of interest relevant to this
424 study.

425 **Acknowledgments.** The Authors would like to express their gratitude to the National Aeronautics
426 and Space Administration (NASA) for providing the SABER data downloaded from the website:
427 <http://saber.gats-inc.com/index.php>.

428 **References**

429 Bague, N., Mbatha, N., Bencherif, H., Loua, R. T., Siva Kumar, V., & Leblanc, T.: Statistical
430 analysis of the mesospheric inversion layers over two symmetrical tropical sites:
431 Reunion (20.8° S, 55.5° E) and Mauna Loa (19.5° N, 155.6° W). In *Annales Geophysicae*,
432 35, 1177-1194, 2017.

433 Bizuneh, C.L., Prakash, R., and Nigussie, M.: Long-term temperature and ozone response to
434 natural drivers in the mesospheric region using 16 years (2005–2020) of TIMED/SABER
435 observation data at 5-15°N. *Advances in Space Research*, 70, 2095–2111,
436 <https://doi.org/10.1016/j.asr.2022.06.051>, 2022.

437 Collins, R. L., Lehmacher, G. A., Larsen, M. F., and Mizutani, K.: Estimates of vertical eddy
438 diffusivity in the upper mesosphere in the presence of a mesospheric inversion layer, *Ann.*
439 *Geophys.*, 29(11), 2019–2029, <http://doi:10.5194/angeo-29-2019-2011>, 2011.

440 Cutler, L. J., Collins, R. L., Mizutani, K., and Itabe, T.: Rayleigh lidar observations of mesospheric
441 inversion layers at Poker Flat, Alaska (65° N, 14° W), *Geophys. Res. Lett.*, 28, 1467–1470,
442 <https://doi.org/10.1029/2000GL012535>, 2001.

443 Dou, X., Li, T., Xu, J., Liu, H. L., Xue, X., Wang, S., Leblanc, T., McDermid, I. S., Hauchecorne,
444 A., Keckhut, P., Bencherif, H., Heinselman, C., Steinbrecht, W., Mlynczak, M. G., and Russell
445 III, J. M.: Seasonal oscillations of middle atmosphere temperature observed by Rayleigh lidars
446 and their comparisons with TIMED/SABER observations, *J. Geophys. Res.*, 114, D20103,
447 <https://doi.org/10.1029/2008JD011654>, 2009.

448 Duck, T. J., Sipler, D. P., and Salah, J. E.: Rayleigh lidar observations of a mesospheric inversion
449 layer during night and day, *Geophys. Res. Lett.*, 28, 3597–3600, 2001.

450 Duck, T. J. and Greene, M. D.: High Arctic observations of mesospheric inversion layers,
451 *Geophys. Res. Lett.*, 31, L02105, <https://doi.org/10.1029/2003GL018481>, 2004.

452 Eckermann, S.D., Hirota, I., and Hocking, W. K.: Gravity wave and equatorial wave morphology
453 of the stratosphere derived from long-term rocket soundings. *Q. J. R. Meteorol. Soc.*, 121, 149
454 186, <http://doi.org/10.1002/qj.49712152108>, 1994.

455 Emanuel, K.A.: *Atmospheric Convection*, Oxford University Press, New York, 580pp, 1994.

456 Fechine, J., Wrasse, C. M., Takahashi, H., Mlynczak, M. G., and Russell, J. M.: Lower-
457 mesospheric inversion layers over Brazilian equatorial region using TIMED/SABER
458 temperature profiles, *Adv. Space Res.*, 41, 1447–1453, [https://doi.org/10.1016/j.asr.2007.](https://doi.org/10.1016/j.asr.2007.04.070)
459 [04.070](https://doi.org/10.1016/j.asr.2007.04.070), 2008.

460 Fritts, D. C., Wang, L., Laughman, B., Lund, T. S., & Collins, R. L.: Gravity wave dynamics in a
461 mesospheric inversion layer: 2. Instabilities, turbulence, fluxes, and mixing. *Journal of*
462 *Geophysical Research: Atmospheres*, 123, 649–670, <https://doi.org/10.1002/2017JD027442>,
463 2018.

464 France, J. A., Harvey, V. L., Randall, C. E., Collins, R. L., Smith, A. K., Peck, E. D., and Fang,
465 X.: A climatology of planetary wave-driven mesospheric inversion layers in the extratropical
466 winter, *J. Geophys. Res.-Atmos.*, 120, 399–413, <https://doi.org/10.1002/2014JD022244>, 2015.

467 Fritts, D. C., and Alexander, M. J.: Gravity wave dynamics and effects in the middle atmosphere,
468 *Rev. Geophys.*, 41, 1003, <https://doi.org/10.1029/2001RG000106>, 2003.

469 Fritts, D. C., Laughman, B., Wang, L., Lund, T. S., & Collins, R. L.: Gravity wave dynamics in a
470 mesospheric inversion layer: 1. Reflection, trapping, and instability dynamics. *Journal of*
471 *Geophysical Research: Atmospheres*, 123, 626-648, <https://doi.org/10.1002/2017JD027440>,
472 2018.

473 Gan, Q., Zhang, S. D., and Yi, F.: TIMED/SABER observations of lower mesospheric inversion
474 layers at low and middle latitudes, *J. Geophys. Res.*, 117, D07109, [https://doi.org/10.1029/2012JD](https://doi.org/10.1029/2012JD017455)
475 [017455](https://doi.org/10.1029/2012JD017455), 2012.

476 Garcia-Comas, M., Lopez-Puertas, M., Marshall, B. T., Winter Steiner, P. P., Funke, B., Bermejo-
477 Pantaleon, D., Mertens, C. J., Remsberg, E. E., Gordley, L. L., Mlynczak, M. G., and Russell III,
478 J. M.: Errors in Sounding of the Atmosphere using Broadband Emission Radiometry (SABER)
479 kinetic temperature caused by non-local-thermodynamic-equilibrium model parameters, *J.*
480 *Geophys. Res.*, 113, D24106, doi: 10.1029/2008JD010105, 2008.

481 Hirota, I.: Climatology of gravity waves in the middle atmosphere. *J. Atmos. Terr. Phys.*, 46, 767–
482 773, <http://doi.org/10.2151/jmsj1965.63.6-1055>, 1984.

483 Hamilton, K.: Climatological Statistics of Stratospheric Inertia-Gravity Waves Deduced from
484 Historical Rocket-sonde Wind and Temperature Data. *J. Geophys. Res.*, 96, 20831–20839,
485 <http://doi.org/10.1029/91JD02188>, 1991.

486 Hauchecorne, A., Chanin, M. L., & Wilson, R.: Mesospheric temperature inversion and
487 gravity wave breaking. *Geophysical Research Letters*, 14(9), 933-936, [https://doi.org/10.1029/
488 GL014i009p00933](https://doi.org/10.1029/GL014i009p00933), 1987.

489 Holton, J. R., Curry, J. A., and Pyle, J. A.: *Encyclopedia of atmospheric sciences*, volume 1.
490 Academic Press, 2003.

491 Holton, J. R.: The influence of gravity wave breaking on the general circulation of the middle
492 atmosphere, *J. Atmos. Sci.*, 40, 2497–2507, 1983.

493 Holton, J. R. and Hakim, G. J.: *An introduction to dynamic meteorology*. Academic Press, 2013.

494 Irving, B. K., Collins, R. L., Lieberman, R. S., Thurairajah, B., and Mizutani, K.: Mesospheric
495 Inversion Layers at Chatanika, Alaska (65°N, 147°W): Rayleigh lidar observations and analysis,
496 *J. Geophys. Res. Atmos.*, 119, 11,235–249, <http://doi:10.1002/2014JD021838>, 2014.

497 John, S.R., Kumar, K. K.: TIMED/SABER observations of global gravity wave climatology and
498 their interannual variability from stratosphere to mesosphere lower thermosphere. *Clim. Dyn.*,
499 39, 1489–1505, <http://doi.org/10.1007/s00382-012-1329-9>, 2012.

500 Leblanc, T., McDerimid, I. S., Hauchecorne, A., and Keck hut, P.: Evaluation of optimization of
501 lidar temperature analysis algorithms using simulated data, *J. Geophys. Res.*, 103, 6177–6187,
502 1998.

503 Leblanc, T., and Hauchecorne, A.: Recent observations of mesospheric temperature inversions, *J.*
504 *Geophys. Res.*, 102, 19471–19482, <https://doi.org/10.1029/97JD01445>, 1997.

505 Lindzen, R. S.: Turbulence and stress due to gravity waves and tidal breakdown, *J. Geophys. Res.*,
506 86, 9707–9714, <https://doi:10.1029/JC086iC10p09707>, 1981.

507 Lingerew, C., Jaya Prakash Raju, U., & Guimarães Santos, C. A.: NN-MLT model prediction for
508 low-latitude region based on artificial neural network and long-term SABER observations. *Earth
509 and Space Science*, 10, e2023EA002930, <https://doi.org/10.1029/2023 EA002930>, 2023.

510 Liu, S-D., and S-S. Liu: *Atmosphere Dynamics*, Peking University Press, Beijing, 2011.

511 Liu, H. L., Hagan, M. E., & Roble, R. G.: Local mean state changes due to gravity wave
512 breaking modulated by the diurnal tide. *Journal of Geophysical Research*, 105(D10),
513 12381-12396, (2000).

514 Liu, H. L., & Hagan, M. E.: Local heating/cooling of Atmospheres. 96(D8), 15297-15309, (1998).
515 Mlynczak, M. G., Marshall, B. T., Martin-Torres, F. J., Russell III, J. M., Thompson, R. E.,
516 Remsberg, E. E., and Gordley, L. L.: Sounding of the Atmosphere using Broadband Emission
517 Radiometry observations of daytime mesospheric O₂ (1Δ) 1.27 μm emission and derivation of
518 ozone, atomic oxygen, and solar and chemical energy deposition rates, 2007.

519 Meriwether, J. W., and Gerrard, A. J.: Mesosphere inversion layers and stratosphere temperature
520 enhancements, *Rev. Geophys.*, 42, RG3003, <http://doi:10.1029/2003RG000133>, 2004.

521 Meriwether, J. W., and Gardner, C. S.: A review of the mesosphere inversion layer phenomenon,
522 *J. Geophys. Res.*, 105, 12 405–12 416, 2000.

523 Nath, O., & Sridharan, S.: Long-term variabilities and tendencies in zonal mean TIMED–SABER
524 ozone and temperature in the middle atmosphere at 10–15°N. *Journal of Atmospheric and Solar-*
525 *Terrestrial Physics*, 120, 1–8, <https://doi:10.1016/j.jastp.2014.08.010>, 2014.

526 Ramesh, K., Sridharan, S.: Large mesospheric inversion layer due to breaking of small scale
527 gravity waves: Evidence from Rayleigh lidar observations over Gadanki (13.51° N, 79.21° E). *J.*
528 *Atmos. Sol. Terr. Phys.* 89, 90–97, <http://doi.org/10.1016/j.jastp.2012.08.011>, 2012.

529 Ramesh, K., Sridharan, S. and Vijaya Bhaskara, S.: Causative mechanisms for the occurrence of a
530 triple-layered mesospheric inversion event over low latitudes, *J. Geophys. Res. Space Physics*,
531 119, 3930–3943, <http://doi:10.1002/2013JA019750>, 2014.

532 Ramesh, K., Sridharan, S., Raghunath, K., and Rao, S. V. B.: A chemical perspective of day and
533 night tropical (10°N–15°N) mesospheric inversion layers, *J. Geophys. Res. Space Physics*, 122,
534 <http://doi:10.1002/2016JA023721>, 2017.

535 Ramesh, K., Sridharan, S., Vijaya Bhaskara Rao, S., Raghunath, K., Bhavani Kumar, K.: Rayleigh
536 lidar observations of mesospheric inversion layers over Gadanki (13.5°N, 79.2° E) and their
537 relation with gravity wave activities. *Indian Journal of Radio and Space Science*, 43, 83-90,
538 2013.

539 Remsberg, E., Lingenfelter, V., Harvey, V., Grose, W., Russell III, J., Mlynczak, M., Gordley, L.,
540 and Marshall, B. T.: The verification of the quality of SABER temperature, geopotential height,
541 and wind fields by comparison with Met Office assimilated analyses, *J. Geophys. Res.*,
542 108(D19), 4628, <https://doi:10.1029/2003JD003720>, 2003.

543 Rezac, L., Kutepov, A., Russell, J.M., Feofilov, A.G., Yue, J., and Goldberg, R.A.: Simultaneous
544 retrieval of T (p) and CO₂ VMR from two-channel non-LTE limb radiances and application to

545 daytime SABER/ TIMED measurements. *J. Atmos. Sol. Terr. Phys* 130–131, 23–42.
546 <https://doi.org/10.1016/j.jastp.2015.05.004>, 2015.

547 Russell, J.M., Mlynczak, M.G., Gordley, L.L., Tansock, J., Esplin, R.: An overview of the SABER
548 experiment and preliminary calibration results. In *Proceedings of the SPIE, 44th Annual*
549 *Meeting, Denver, CO, USA, 3756, 277–288, 1999.*

550 Schmidlin, F. J.: Temperature inversions near 75 km. *Geophysical Research Letters*, 3(3),
551 173-176, (1976).

552 Sica, R. J., Argall, P. S., Shepherd, T. G., and Koshyk, J. N.: Model-measurement comparison of
553 mesospheric temperature inversions, and a simple theory for their occurrence, *Geophys. Res.*
554 *Lett.*, 34, L23806, <https://doi:10.1029/2007GL030627>, 2007.

555 Sivakandan, M., Kapasi, D., and Taori, A.: The occurrence altitudes of middle atmospheric
556 temperature inversions and mesopause over low-latitude Indian sector, *Ann. Geophys.*, 32,
557 967–974, <https://doi.org/10.5194/angeo-32-967-2014>, 2014.

558 Siva Kumar, V., Bhavani Kumar, Y., Raghunath, K., Rao, P. B., Krishnaiah, M., Mizutani, K.,
559 Aoki, T., Yasui, M., and Itabe, T.: Lidar measurements of mesospheric temperature inversion at
560 a low latitude, *Ann. Geophys.*, 19, 1039–1044, <https://doi.org/10.5194/angeo-19-1039-2001>,
561 2001.

562 Sridharan, S., Sathishkumar, S., and Gurubaran, S.: Influence of gravity waves and tides on
563 mesospheric temperature inversion layers: simultaneous Rayleigh lidar and MF radar
564 observations, *Ann. Geophys.*, 26, 3731–3739, 2008.

565 Singh, R. P., & Pallamraju, D.: Mesospheric temperature inversions observed in OH and O2
566 rotational temperatures from Mount Abu (24.6°N, 72.8°E), India. *Journal of Geophysical*
567 *Research: Space Physics*, 123, 8823–8834, <https://doi.org/10.1029/2018JA025703>, 2018.

568 Smith, A.: Global Dynamics of the MLT, *Surv. Geophys*, 33, 1177–1230, <https://doi.org/10.1007/s10712-012-9196-9>, 2012.

570 Szewczyk, A., Strelnikov, B., Rapp, M., Strelnikova, I., Baumgarten, G., Kaifler, N., Dunker, T.,
571 and Hoppe, U. P.: Simultaneous observations of a Mesospheric Inversion Layer and turbulence
572 during the ECOMA-2010 rocket campaign, *Ann. Geophys.*, 31, 775–785, [http://doi:10.5194/](http://doi:10.5194/angeo-31-775-2013)
573 [angeo-31-775-2013](http://doi:10.5194/angeo-31-775-2013), 2013.

574 Vadas, S. L., and Fritts, D. C.: Thermosphere responses to gravity waves: Influences of increasing
575 viscosity and thermal diffusivity, *J. Geophys. Res.*, VOL. 110, D15103, doi: 10.1029/2004JD
576 005574, 2005.

577 Wang, L., Geller, M.A., Alexander, M.J.: Spatial and Temporal Variations of Gravity Wave
578 Parameters. Part I: Intrinsic Frequency, Wavelength, and Vertical Propagation Direction. *J.*
579 *Atmos. Sci.*, 62, 125–142, <http://doi.org/10.1029/2010JD013860>, 2005.

580 Wang, L., and Alexander, M.J.: Global estimates of gravity wave parameters from GPS radio
581 occultation temperature data. *J. Geophys. Res.* 115, D21122, [http://doi.org/10.1029/2010J
D013860](http://doi.org/10.1029/2010J
582 D013860), 2010.

583 Walterscheid, R. L., and Hickey, M. P.: Gravity wave ducting in the upper mesosphere and lower
584 thermosphere duct system, *J. Geophys. Res.*, 114, D19109, <http://doi:10.1029/2008JD 011269>,
585 2009.

586 Yuan, T., Pautet, P. D., Zhao, Y., Cai, X., Criddle, N. R., Taylor, M. J., and Pendleton, W. R.:
587 Coordinated investigation of mid-latitude upper mesospheric temperature inversion layers and
588 the associated gravity wave forcing in Logan, Utah, *J. Geophys. Res. Atmos.*, 119, 3756–3769,
589 <http://doi:10.1002/2013JD020586>, 2014.